Boundary element analysis of three-dimensional mixed-mode thermoelastic crack problems using the interaction and energy domain integrals

R. Balderrama[1], A. P. Cisilino[2, *, †] and M. Martinez[1]

[1]*Mechanical Engineering School, Universidad Central de Venezuela, Caracas, Venezuela*
[2]*Welding and Fracture Division—INTEMA-CONICET, Universidad Nacional de Mar del Plata,*
Av. Juan B. Justo 4302, (7600) Mar del Plata, Argentina

SUMMARY

A three-dimensional boundary element method (BEM) implementation of the interaction integral methodology for the numerical analysis of mixed-mode three-dimensional thermoelastic crack problems is presented in this paper. The interaction integral is evaluated from a domain representation naturally compatible with the BEM, since stresses, strains, temperatures and derivatives of displacements and temperatures at internal points can be evaluated using the appropriate boundary integral equations. Several examples are analysed and the results compared with those available in the literature to demonstrate the efficiency and accuracy of the implementation to solve straight and curved crack-front problems. Copyright © 2007 John Wiley & Sons, Ltd.

1. INTRODUCTION

Whenever the expansion or contraction that would normally result from the heating or cooling of a body is prevented, stresses are developed, which are called thermal or temperature stresses. The study of thermal stresses is stimulated by the need to assess the engineering integrity and life expectancy of thermally stressed components, either under service conditions or during the design

---

*Correspondence to: A. P. Cisilino, Welding and Fracture Division—INTEMA-CONICET, Universidad Nacional de Mar del Plata, Av. Juan B. Justo 4302, (7600) Mar del Plata, Argentina.
†E-mail: cisilino@fi.mdp.edu.ar

stage. In particular, the fracture mechanics analysis becomes an increasingly important factor in the design of components of modern structures and devices that undergo heating, such as steam pipes and vessels, nuclear reactors, combustion chambers, cutting tools and electronic devices.

Over the years, much work has been done to evaluate stress intensity factors for these problems, resulting in collections of results published in handbook form [1, 2]. However, most of these solutions are restricted to regular cracks in infinite or semi-finite solids and two-dimensional simple crack geometries. While two-dimensional analyses are usually sufficient to characterize through-thickness cracks, part-through cracks, which are the most common type of crack defects found in service conditions, have an inherently three-dimensional character. The solution of complicated three-dimensional crack problems usually requires numerical techniques such as the finite element method (FEM) and the boundary element method (BEM).

The attraction of the BEM can be largely attributed to the reduction in the dimensionality of the problem; for three-dimensional problems only the surface of the domain needs to be discretized [3]. This means that, when compared with FEM domain-type analysis, a boundary analysis results in a substantial reduction in data preparation. At the same time, and due to the inherent characteristics of its formulation, BEM provides very accurate results for problems containing strong geometrical discontinuities. This makes BEM a powerful numerical tool for modelling crack problems [4]. In particular, thermoelastic BEM formulations have been presented, among others, by Raveendra and Banerjee [5], Mukherjee *et al.* [6], Prassad *et al.* [7] and dell'Erba and Aliabadi [8, 9].

There exist a variety of methods for the evaluation of stress intensity factors using boundary elements, such as the extrapolation of displacements or stress, special crack tip elements, the subtraction of singularity technique, the strain energy release rate and J-integral methods [10]. Techniques based on the extrapolation of displacements and stresses are easy to implement, but they require a very high level of mesh refinement in order to obtain accurate results. Alternating and virtual crack extension methods are also computationally expensive, as they require multiple computer runs to solve the problem. On the other hand, path-independent integrals, being an energy approach, eliminate the need to solve local crack tip fields accurately, since if integration domains are defined over a relatively large portion of the mesh an accurate modelling of the crack tip is unnecessary because the contribution to J of the crack tip fields is not significant.

The J-integral introduced by Rice [11] characterizes the crack-driving force for two-dimensional problems in the absence of body forces. Therefore, for general three-dimensional problems involving cracks of arbitrary shape subjected to thermal loadings an alternative form for J is needed. Three basic schemes have evolved for the numerical computation of the J-integral in three dimensions: virtual crack extension methods [12, 13], generalization of Rice's contour integral [14] and domain integral methods [15]. Generalizations of the J-integral concept to account for thermal stresses have been proposed among others by Blackburn [16], Ainsworth *et al.* [17], Wilson and Yu [18], Kishimoto *et al.* [19] and Auki *et al.* [20]. The generalization of the J-integral to account for thermal stresses results in most cases in an expression containing two terms: a line integral defined along a closed contour around the crack front and a surface integral defined over the area enclosed by the line contour [18–20]. The J-integral due to Kishimoto *et al.* [19] was implemented using BEM by Prasad *et al.* [7] for the analysis of two-dimensional thermoelastic problems. Its extension to three dimensions was presented by dell'Erba and Aliabadi [8, 9]. Although the bulk of fracture mechanics literature is concerned with the first mode of crack deformation, there are practical engineering problems that involve mixed-mode conditions. Of the above cited papers, dell'Erba and Aliabadi [8, 9] propose a method for decoupling the J-integral for three-dimensional mixed-mode cracks in which the symmetric and antisymmetric parts of the displacement, strain

and stress fields are separated. It is worth noting that the method due to dell'Erba and Aliabadi [8, 9] is based on the work by Rigby and Aliabadi [21], who gave the proper decomposition of the crack stress field in their symmetric and antisymmetric parts, by showing that the expressions used in previous papers were incorrect.

Among the available methods for calculating fracture parameters, the energy domain integral (EDI) has shown to be well suited for three-dimensional BEM analysis. Applications of the EDI to solve three-dimensional crack problems using the BEM have been reported by Cisilino *et al.* for elasticity [22], elastoplasticity [23], fibre–matrix interfaces in composite materials [24] and thermoelasticity [25]. The EDI is versatile and efficient and relatively simple to implement numerically. To develop the domain integral the EDI incorporates an auxiliary function q, which can be interpreted as a virtual crack-front advance. This makes the EDI similar to the virtual crack extension technique [26, 27], but has the advantage that only one computer run is necessary to evaluate the point-wise energy release rate along the complete crack front.

Interaction integral methods are perhaps the most accurate approach to extract mixed-mode, stress intensity factors [28]. These methods are based on the superposition of two equilibrium states, given by the actual problem solution and a set of auxiliary known solutions. William's solution [29] for the two-dimensional asymptotic stress and displacement fields in the vicinity of a crack represents a widely used auxiliary field. Numerical evaluation of this interaction integral fits conveniently into existing domain-integral procedures for J-computation, thereby providing a readily implemented, robust and accurate tool. Interaction integrals have been extensively implemented using FEM, with applications in two and three dimensions for cracks in homogeneous bodies [28, 30–32] and interface cracks [33, 34]. Nakamura and Parks [35] discuss the formulation of an interaction integral for thermal and body-force loads. Interaction integrals have been implemented using BEM by Miyazaki *et al.* [36] and by Cisilino and Ortiz [37] for two- and three-dimensional cracks in isotropic materials, respectively, and by Ortiz and Cisilino [38] for three-dimensional interface cracks.

This work presents a BEM domain formulation of the M_1-interaction integral of Knowles and Sternberg [39] for the computation of mixed-mode stress intensity factors along three-dimensional crack fronts in thermally stressed bodies. The domain representation of the interaction integral is presented in a straightforward approach, followed by the basis of the BEM formulation and the M_1-integral implementation. Several examples are analysed to demonstrate the efficiency and accuracy of the implementation.

2. THE ENERGY DOMAIN INTEGRAL

The formulation of the EDI is presented next, following the work by Shih *et al.* [15]. Consider for this purpose a three-dimensional crack front with a continuously turning tangent as depicted in Figure 1(a). Define a local coordinate system x^* at position η, where the crack energy release rate is evaluated, given by x_1^* normal to the crack front, x_2^* normal to the crack plane and x_3^* tangential to the crack front.

The energy release rate $G(\eta)$ due to crack extension in its own plane along a three-dimensional crack front takes the form (see Figure 1)

$$G(\eta) = \lim_{C \to 0} \xi_k(\eta) \int_{C(\eta)} (w \cdot \delta_{ki} - \sigma_{ij}^* u_{j,k}^*) n_i \, \mathrm{d}C \tag{1}$$
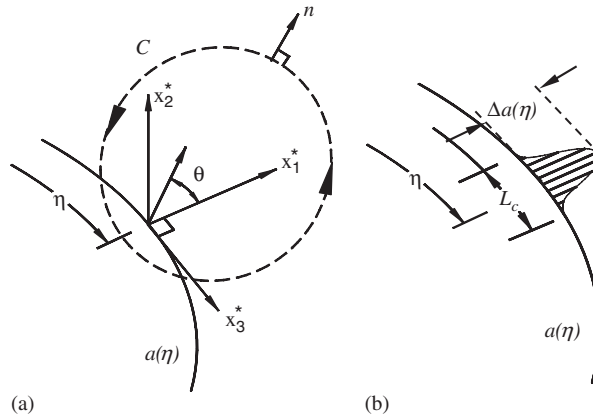
Figure 1. (a) Definition of the local orthogonal Cartesian coordinates at point η on the crack front and (b) virtual crack-front advance.

where w is the strain energy density, σ_{ij}^* and $u_{j,k}^*$ are Cartesian components of stress and displacement derivatives expressed in the local system x^*, $\xi_k(\eta)$ is the unit outward normal to the crack front in the local crack plane x_1^*–x_3^*, n_i is the unit vector normal to the contour $C(\eta)$ (which lies in the x_1^*–x_2^* plane) and $\mathrm{d}C$ is the differential of the arc length C. It is worth noting that, although Equation (1) comes from a two-dimensional analysis, it applies to the three-dimensional case, as in the limit as $C \to 0$ plane strain conditions prevail so that three-dimensional fields approach the plane problem.

Within the framework of uncoupled thermoelasticity, the strain is written as the sum of an elastic part ε_{ij}^e and a thermal part

$$\varepsilon_{ij} = \varepsilon_{ij}^e + \alpha\theta\delta_{ij} \tag{2}$$

where α is the coefficient of linear expansion and θ is the temperature. If we make the additional restriction that thermal strains are bounded, a definition of w which can be used in Equation (1) is

$$w(\varepsilon_{ij}, \theta) = \int_0^{\varepsilon_{ij}^m} \sigma_{ij} \, \mathrm{d}\varepsilon_{ij}^m \tag{3}$$

where $\varepsilon_{ij}^m = \varepsilon_{ij} - \alpha\theta\delta_{ij}$ are the mechanical strains.

In order to derive the equivalent domain representation of Equation (1), we consider a small segment L_c of the crack front that lies in the local x_1^*–x_3^* plane as shown in Figure 1(b). Next, we assume that the segment undergoes a virtual crack advance in the plane of the crack, and we define the magnitude of the advance at each point η as $\Delta a(\eta)$. Note that $\Delta a(\eta)$ varies continuously along L_c and vanishes at each end of the segment. Now let

$$\overline{G}(\eta) = \int_{L_C} G(\eta)\Delta a(\eta) \, \mathrm{d}\eta \tag{4}$$

where $G(\eta)$ is the integral defined in Equation (1). Note that while $G(\eta)$ belongs to the point-wise energy release rate, $\overline{G}$ gives the total energy released when the finite segment L_c undergoes the virtual crack advance.
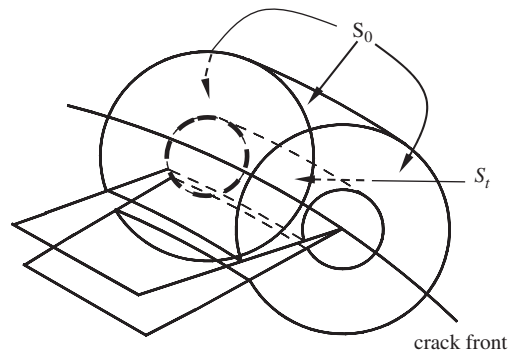
Figure 2. Tubular domain surrounding a segment of the crack front.

The appropriate domain form of the point-wise crack-tip contour integral can be obtained from Equation (2) by considering a tubular domain V surrounding the crack segment (see Figure 2). As shown in the figure, the surface S_t is formed by translating the contour C along the segment L_c, and S_o stands for the outer surface of V including the ends. Next an auxiliary function φ is introduced, which is sufficiently smooth in V and is defined on the surfaces of V as follows:

$$\varphi_k = \begin{cases} \Delta a(\eta) \cdot \xi_k(\eta) & \text{on } S_t \\ 0 & \text{on } S_0 \end{cases} \tag{5}$$

Finally, in the limit as the tubular surface S_t is shrunk onto the crack segment L_c, and after applying the divergence theorem, the domain integral is obtained:

$$\overline{G} = \int_V \{ [\sigma_{ij}^* u_{j,k}^* - w \cdot \delta_{ki}] \varphi_{k,i} + \alpha \sigma_{ii}^* \theta_{,k} \varphi_k \} \, \mathrm{d}V \tag{6}$$

In the evaluation of the energy release rate, the integral given by Equation (6) reduces to the domain representation of the familiar J-integral. A simple relationship between $J(\eta)$ and $\overline{G}$ can be obtained if it is assumed that $\overline{G}$ is constant along the segment L_c. It follows directly from Equation (4) that

$$J(\eta) = \frac{\overline{G}}{\int_{L_C} \Delta a(\eta) \, \mathrm{d}\eta} \tag{7}$$

Finally, it is worth mentioning that the above derivation of the EDI assumes the absence of crack-face tractions. If present, an extra term needs to be included in Equation (6). For a more comprehensive derivation of the EDI, the reader is referred to [15].

3. THE INTERACTION INTEGRAL

In this section, the interaction or M_1-integral methodology for decoupling three-dimensional mixed-mode stress intensity factors is presented. The M_1-integral is based on the principle of superposition. Let us consider two equilibrium states with field variables denoted by superscripts (1) and (2),

respectively. Superposition of the two equilibrium states leads to another one, $(1 + 2)$. Then the stress intensity factors $K_j^{(1+2)}$ can be written as

$$K_j^{(1+2)} = K_j^{(1)} + K_j^{(2)} \quad (j = \text{I, II, III}) \tag{8}$$

The stress intensity factors can be related to the J-integral in a plane-strain condition as follows:

$$J = J_\text{I} + J_\text{II} + J_\text{III} = \frac{1}{E}(K_\text{I}^2 + K_\text{II}^2) + \frac{K_\text{III}^2}{2\mu} \tag{9}$$

where E is the Young's modulus and μ is the shear modulus. Using Equation (9), the J-integral for the superimposed state $(1 + 2)$ can be written as

$$J^{(1+2)} = \frac{1}{E}[(K_\text{I}^{(1+2)})^2 + (K_\text{II}^{(1+2)})^2] + \frac{(K_\text{III}^{(1+2)})^2}{2\mu}$$

$$= J^{(1)} + J^{(2)} + \frac{2}{E}(K_\text{I}^{(1)}K_\text{I}^{(2)} + K_\text{II}^{(1)}K_\text{II}^{(2)}) + \frac{K_\text{III}^{(1)}K_\text{III}^{(2)}}{\mu} \tag{10}$$

Then, the M_1-integral is defined as

$$\frac{2}{E}(K_\text{I}^{(1)}K_\text{I}^{(2)} + K_\text{II}^{(1)}K_\text{II}^{(2)}) + \frac{K_\text{III}^{(1)}K_\text{III}^{(2)}}{\mu} = J^{(1+2)} - J^{(1)} - J^{(2)} = M_1 \tag{11}$$

Using Equation (6), a domain representation of the M_1-integral can be obtained as follows:

$$M_1 = \int_V \{(\sigma_{ij}^{*(1)}u_{j,k}^{*(2)} + \sigma_{ij}^{*(2)}u_{j,k}^{*(1)} - \sigma_{ij}^{*(1)}\varepsilon_{ij}^{*(2)}\delta_{ki})\varphi_{,i} + \sigma_{nn}^{*(2)}\alpha\theta_{,k}^{(1)}\varphi_k\} \, \mathrm{d}V \tag{12}$$

Note that Equation (12) accounts for the thermal effects of equilibrium state (1) only. For decoupling the mixed-mode stress intensity factors, the problem under consideration is selected as equilibrium state (1), so that the field variables $\sigma_{ij}^{(1)}$, $u_{j,k}^{(1)}$ and $\theta_{,k}^{(1)}$ will be obtained in this work from the results of a boundary element analysis.

The well-known plane-strain solutions for the asymptotic crack-tip fields with prescribed stress intensity factors K_I, K_II and K_III due to Williams [29] are selected as equilibrium state (2). Then the field variables related to the equilibrium state (2), $\sigma_{ij}^{(2)}$, $u_{j,k}^{(2)}$ and $\varepsilon_{ij}^{(2)}$ are calculated from these asymptotic solutions.

Sih [40] showed that the thermal flux and the stress field are both singular at crack tips. In cases where the temperature is antisymmetric with respect to the crack, the flux singularity is similar to the stress singularity. Moreover, thermal loads create a similar stress distribution as that of a mechanical load. Thus, thermal loads produce a stress singularity at the crack tip, which leads to stress intensity factors. Hence, the stress intensity factors due to mechanical and thermal loads can be superimposed. On the other hand, it is important to point out that the above expression for the M_1-integral is strictly valid for straight crack fronts only. For a curved crack front, the two-dimensional asymptotic Williams solutions do not satisfy equilibrium or strain–displacement compatibility when expressed in curvilinear coordinates, thereby leading to additional terms in the interaction integral [28, 31, 34]. In a recent paper, Walters et al. [28] investigated the effect of the curvature terms on the accuracy of stress intensity factor computations. They demonstrated

that the omission of the curvature terms not only simplifies the computations, but it also allows yielding stress intensity factor results with reasonable levels of mesh discretization. Based on this antecedent, it was decided to exclude the curvature terms from the present implementation. Furthermore, the significance of the neglected terms will be assessed in the Examples section by verifying the path independence of the computed results.

Finally, the M_1-integral defined in Equation (12) can be calculated using the field variables related to equilibrium states (1) and (2). By using three sets of asymptotic solutions:

$$
\begin{aligned}
K_{\mathrm{I}}^{(2)} &= 1, \quad K_{\mathrm{II}}^{(2)} = 0, \quad K_{\mathrm{III}}^{(2)} = 0 \\
K_{\mathrm{I}}^{(2)} &= 0, \quad K_{\mathrm{II}}^{(2)} = 1, \quad K_{\mathrm{III}}^{(2)} = 0 \\
K_{\mathrm{I}}^{(2)} &= 0, \quad K_{\mathrm{II}}^{(2)} = 0, \quad K_{\mathrm{III}}^{(2)} = 1
\end{aligned}
\tag{13}
$$

Thus, it is possible to obtain the stress intensity factor solutions for individual modes from Equation (11) as follows:

$$
K_{\mathrm{I}}^{(1)} = \frac{M_1^a E}{2}, \quad K_{\mathrm{II}}^{(1)} = \frac{M_1^b E}{2}, \quad K_{\mathrm{III}}^{(1)} = M_1^c \mu
\tag{14}
$$

where M_1^a, M_1^b and M_1^c are the values of the M_1-integral calculated using the three sets of asymptotic solutions.

4. THE DUAL BOUNDARY ELEMENT METHOD FOR THERMOELASTICITY

Although the conventional BEM is efficient in carrying out general stress analysis, it is not possible to use it directly for general mixed-mode crack problems in single-region analysis. The coincidence of the crack surfaces makes the collocation points on two surfaces identical, leading to a mathematical degeneration [4]. Among the special techniques devised to overcome this difficulty, the dual boundary element method (DBEM) is the more general and versatile. The DBEM overcomes the problem of the coincident points on the crack surfaces by introducing additional independent boundary integral equations: the flux and traction equations. The DBEM for thermoelasticity used in this work follows that proposed by dell'Erba and Aliabadi [8].

Consider a linear-elastic, isotropic and homogeneous body occupying a domain $\Omega(X)$ enclosed by a boundary $\Gamma(x)$ as illustrated in Figure 3(a). The two governing equations for steady-state thermoelasticity are the Laplace and the Navier equations which can be written as follows:

$$
\theta_{,kk} = 0
\tag{15}
$$

$$
\mu u_{i,jj} + \frac{\mu}{(1-2v)} u_{j,ij} - \frac{2\mu(1+v)}{(1-2v)} \alpha \theta_{,i} = 0
\tag{16}
$$

where θ is the temperature and u_i are the displacement components, μ is the shear modulus, v is the Poisson ratio and α is the coefficient of linear thermal expansion. Equations (15) and (16) are solved subject to boundary conditions in temperatures θ, fluxes q, displacements u and tractions t (see Figure 3(a)).

The dual boundary integral equations on which the thermoelastic formulation of the DBEM is based are the temperature and flux boundary integral equations for the solution of the Laplace
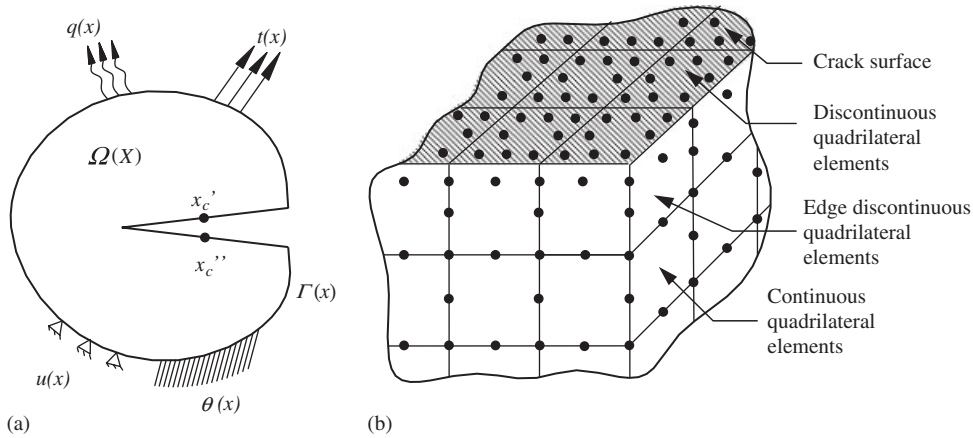
Figure 3. (a) General cracked body with mechanical and thermal boundary conditions
and (b) crack discretization strategy.

equation, and the displacement and traction integral equations for the solution of the Navier equation. The boundary integral temperature equation relating the boundary temperature $\theta(x)$ with the boundary fluxes $q(x)$ can be written as

$$c(x')\theta(x') - \int_\Gamma q^*(x', x)\theta(x)\,\mathrm{d}\Gamma = -\int_\Gamma \theta^*(x', x)q(x)\,\mathrm{d}\Gamma \tag{17}$$

where $c(x')$ depends on the local geometry of the boundary surface at the position of point x'; and $\theta^*(x', x)$ and $q^*(x', x)$ are the temperature and flux fundamental solutions at a boundary point x due to a unit source placed at location x'. Expressions for the fundamental solutions $\theta^*(x', x)$ and $q^*(x', x)$ are given in the Appendix.

Assuming continuity of both temperatures and fluxes at x' on a smooth boundary, the boundary flux integral equation is obtained by differentiating Equation (17):

$$c(x')q(x') + n_i(x')\fint_\Gamma \theta_i^{**}(x', x)q(x)\,\mathrm{d}\Gamma = n_i(x')\fiint_\Gamma q_i^{**}(x', x)\theta(x)\,\mathrm{d}\Gamma \tag{18}$$

where $n_i(x')$ denotes the component of the outward unit normal to the boundary at x'. Expressions for the kernels $\theta_i^{**}(x', x)$ and $q_i^{**}(x', x)$ are given in the Appendix. The symbols $\fint$ and $\fiint$ stand for the Cauchy and Hadammard principal value integrals.

If Equations (17) and (18) are used for collocation on coincident points on the crack surfaces (points x_c' and x_c'' in Figure 3(b)), the temperature and flux boundary integral equations can be written as

$$\frac{1}{2}\theta(x_c') + \frac{1}{2}\theta(x_c'') + \int_\Gamma q^*(x_c', x)\theta(x)\,\mathrm{d}\Gamma = \int_\Gamma \theta^*(x_c', x)q(x)\,\mathrm{d}\Gamma \tag{19}$$

and

$$\frac{1}{2}q(x_c') - \frac{1}{2}q(x_c'') + n_i(x_c'')\fint_\Gamma \theta_i^{**}(x_c'', x)q(x)\,\mathrm{d}\Gamma = n_i(x_c'')\fiint_\Gamma q_i^{**}(x_c'', x)\theta(x)\,\mathrm{d}\Gamma \tag{20}$$

where the normal vectors $n_i(x') = -n_i(x'')$ are assumed on the crack surface. At the same time, it is also assumed that the crack surfaces at the position x'_c and x''_c are always smooth. The latter assumption yields $c(x') = \frac{1}{2}$ in Equations (17) and (18).

Similar to the boundary integral temperature equation, the displacement boundary integral equation relates the displacements $u_j(x)$ with the boundary tractions $t_j(x)$, temperatures $\theta(x)$ and fluxes $q(x)$:

$$c_{ij}(x')u_j(x') + \int_\Gamma T_{ij}(x', x)u_j(x)\,\mathrm{d}\Gamma - \int_\Gamma \overline{P}_i(x', x)\theta(x)\,\mathrm{d}\Gamma$$

$$= \int_\Gamma U_{ij}(x', x)t_j(x)\,\mathrm{d}\Gamma - \int_\Gamma \overline{Q}_i(x', x)q(x)\,\mathrm{d}\Gamma \tag{21}$$

where $U_{ij}(x', x)$ and $T_{ij}(x', x)$ are the Kelvin traction and displacement fundamental solutions for elasticity, and $\overline{P}_i(x', x)$ and $\overline{Q}_i(x', x)$ are the fundamental fields that account for the thermal expansion (see Appendix).

Assuming continuity of both strains and tractions at x' on a smooth boundary, the boundary traction integral equation is obtained by differentiating Equation (21) and by applying the material constitutive relationships

$$\frac{1}{2}t_j(x') + n_j(x')\!\!\fint_\Gamma T_{kij}(x', x)u_k(x)\,\mathrm{d}\Gamma - n_j(x')\int_\Gamma \overline{P}_{ij}(x', x)\theta(x)\,\mathrm{d}\Gamma + \frac{\mu(1+v)}{(1-2v)}\alpha n_i(x')\theta(x')$$

$$= n_j(x')\int_\Gamma U_{kij}(x', x)t_k(x)\,\mathrm{d}\Gamma - n_j(x')\int_\Gamma \overline{Q}_{ij}(x', x)q(x)\,\mathrm{d}\Gamma \tag{22}$$

where the kernels $T_{kij}(x''_c, x)$, $U_{kij}(x''_c, x)$, $\overline{P}_{ij}(x''_c, x)$ and $\overline{Q}_{ij}(x''_c, x)$ contain derivatives of the fundamental fields in Equation (21) together with elastic constants.

If as it has been done with their thermal counterparts Equations (21) and (22) are used for collocation on coincident points on the crack surfaces, then, the displacement and traction boundary integral equations can be written as

$$\frac{1}{2}u_j(x'_c) + \frac{1}{2}u_j(x''_c) + \int_\Gamma T_{ij}(x', x)u_j(x)\,\mathrm{d}\Gamma - \int_\Gamma \overline{P}_i(x', x)\theta(x)\,\mathrm{d}\Gamma$$

$$= \int_\Gamma U_{ij}(x', x)t_j(x)\,\mathrm{d}\Gamma - \int_\Gamma \overline{Q}_i(x', x)q(x)\,\mathrm{d}\Gamma \tag{23}$$

and

$$\frac{1}{2}t_j(x''_c) - \frac{1}{2}t_j(x'_c) + n_j(x''_c)\!\!\fint_\Gamma T_{kij}(x''_c, x)u_k(x)\,\mathrm{d}\Gamma - n_j(x''_c)\int_\Gamma \overline{P}_{ij}(x''_c, x)\theta(x)\,\mathrm{d}\Gamma$$

$$+ \frac{\mu(1+v)}{(1-2v)}\alpha n_i(x''_c)\theta(x''_c)$$

$$= n_j(x''_c)\int_\Gamma U_{kij}(x''_c, x)t_k(x)\,\mathrm{d}\Gamma - n_j(x''_c)\int_\Gamma \overline{Q}_{ij}(x''_c, x)q(x)\,\mathrm{d}\Gamma \tag{24}$$

Following dell'Erba and Aliabadi [8], the general discretization strategy can be summarized as follows (see Figure 3(b)):

- Crack surfaces are discretized using 8-node discontinuous quadrilateral elements in order to ensure the continuity requirements of the field variables for the existence of the flux and traction equations.
- Continuous elements are used over the remaining model boundary, except at the intersection of the crack with the boundary surface. Edge discontinuous elements are employed in this region in order to avoid common nodes at the intersection.
- The temperature integral equation (19) and the displacement integral equation (23) are applied for collocation on one of the crack surfaces.
- The flux integral equation (20) and the traction integral equation (24) are applied for collocation on the opposite crack surface.
- The temperature integral equation (17) and the displacement integral equation (21) are applied for collocation on all other surfaces.

This simple strategy is robust and allows the DBEM to effectively model general crack problems. Crack tips, crack edge corners and crack kinks do not require special treatment, since they are not located at nodal points where the collocation is carried out.

5. STRESSES, STRAINS, AND DISPLACEMENT AND TEMPERATURE DERIVATIVES

5.1. Internal points

As it has been stated in Sections 2 and 3, the computation of the M_1-integral requires the displacement and temperature derivatives, $u_{i,j}$ and $\theta_{,k}$, and the stress and strain fields, σ_{ij} and ε_{ij}, to be known within the integration volume V. Although these quantities must be expressed in the local crack-front coordinate system, in this work, and for the sake of simplicity, they are first computed in the global system and then transformed to the local crack-front coordinate system. Bearing this in mind, and in order to integrate the computation of the J-integral into the DBEM formulation, derivatives of the displacements at internal points X' are obtained from their boundary integral representations. Thus, the integral equation for the displacement and temperature derivatives results from the analytical differentiation of the internal counterparts of Equations (17) and (21):

$$\theta_{,k}(X') = \int_\Gamma q_{,k}^{**}(X', x)\theta(x)\,\mathrm{d}\Gamma - \int_\Gamma \theta_{,k}^{**}(X', x)q(x)\,\mathrm{d}\Gamma \tag{25}$$

and

$$u_{i,k}(X') = -\int_\Gamma T_{ij,k}(X', x)u_j(x)\,\mathrm{d}\Gamma + \int_\Gamma \overline{P_{i,k}}(X', x)\theta(x)\,\mathrm{d}\Gamma$$

$$+ \int_\Gamma U_{ij,k}(X', x)t_j(x)\,\mathrm{d}\Gamma - \int_\Gamma \overline{Q_{i,k}}(X', x)q(x)\,\mathrm{d}\Gamma \tag{26}$$

where the kernels $q_{,k}^{**}(X', x)$, $\theta_{,k}^{**}(X', x)$, $T_{ij,k}(X', x)$, $U_{ij,k}(X', x)$, $\overline{P_{i,k}}(X', x)$ and $\overline{Q_{i,k}}(X', x)$ are the derivatives of the fundamental solutions.

Once the displacement derivatives $u_{j,k}$ are known, stresses σ_{ij} and strains ε_{ij} are computed using basic continuum mechanics relationships:

$$\varepsilon_{ij} = \tfrac{1}{2}(u_{i,j} + u_{j,i}) + \alpha\theta\delta_{ij} \tag{27}$$

$$\sigma_{ij} = \frac{E}{1+v}\left[\varepsilon_{ij} + \frac{v}{1-2v}\varepsilon_{kk}\delta_{ij}\right] - \frac{E}{1-2v}\alpha\theta\delta_{ij} \tag{28}$$

5.2. Boundary points

Temperature and displacement derivatives $\theta_{,k}$ and $u_{i,j}$ at boundary nodes could be obtained from Equations (25) and (26) in a similar way as their internal counterparts, by taking the limit of Equations (25) and (26) as point X' moves to the boundary, i.e. $X' \to x'$. However, this procedure is computationally expensive because of the occurrence of hypersingular integrands. To avoid this difficulty, stresses and strains, as well as the displacements and temperatures on the model surface are evaluated in this work from the boundary displacements, tractions, temperatures and fluxes following a procedure similar to that used in FEM computations. Consider for this purpose a local Cartesian system (x_1^0, x_2^0, x_3^0) such that x_3^0 is the unit vector in the normal direction to the boundary element (see Figure 4). If σ_{ij}^0 and t_j^0 are stresses and tractions in the local system, stress components in the normal direction can be written as

$$\sigma_{i3}^0 = t_i^0 \tag{29}$$

The remaining stress tensor components, σ_{11}^0, σ_{12}^0 and σ_{22}^0 can be expressed in terms of t_3^0 and the tangential strain tensor components ε_{11}^0, ε_{12}^0 and ε_{22}^0, by eliminating ε_{33}^0 from the general expression of Hooke's law. Thus,

$$\sigma_{11}^0 = \frac{1}{1-v}[vt_3^0 + 2\mu(\varepsilon_{11}^0 + v\varepsilon_{22}^0) - (1+v)\alpha\theta]$$

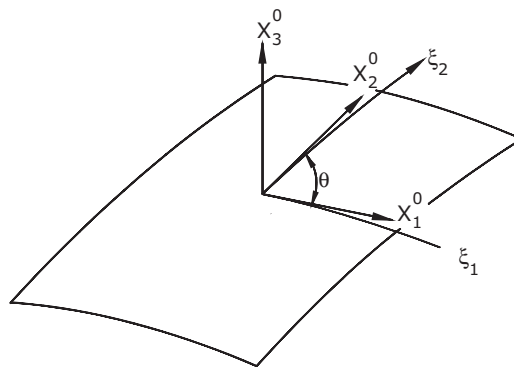Figure 4. Orthogonal coordinate system at the surface.

$$\sigma_{22}^0 = \frac{1}{1-v}[vt_3^0 + 2\mu(\varepsilon_{22}^0 + v\varepsilon_{11}^0) - (1+v)\alpha\theta]$$

$$\sigma_{12}^0 = 2\mu\varepsilon_{12}^0 \tag{30}$$

Strain components ε_{ij}^0 can be obtained using Equation (27), now applied in the local coordinate system. It is worth noting that displacement derivatives in Equation (27) are initially evaluated in the intrinsic element directions (ξ_1, ξ_2) and then converted to the local coordinate system x^0, since, as is usual in BEM, boundary displacements are approximated in terms of the piecewise parametric representation (shape functions) of intrinsic coordinates:

$$u_i(\xi_1, \xi_2) = \sum_{n=1}^{8} \Phi^n(\xi_1, \xi_2) u_i^n \tag{31}$$

where Φ^n are the shape functions and u_i^n are the nodal values of the displacements. From (31) it follows that

$$\frac{\partial u_i}{\partial \xi_j} = \sum_{n=1}^{8} \frac{\partial \Phi^n}{\partial \xi_j} u_i^n \tag{32}$$

Finally, the derivatives of the displacements in the global system are computed. Using chain differentiation, derivatives of the displacements in the global system, $u_{i,m}$, can be related to the derivatives of the displacements in the intrinsic boundary element directions, $\partial u_i/\partial \xi_j$, as follows:

$$\frac{\partial u_i}{\partial \xi_j} = \frac{\partial u_i}{\partial x_m} \frac{\partial x_m}{\partial \xi_j} \tag{33}$$

where $\partial x_m/\partial \xi_j$ is the Jacobian matrix of the transformation. The nine components of the displacement derivatives $u_{i,m}$ can be retrieved by solving for each case a system of equations constructed using expressions (33). For further details the reader is referred to the works by Cisilino *et al.* [22–25].

A similar procedure can be employed for the computation of the temperature derivatives on the model boundary. Following the same approach used for the displacements, temperature derivatives in the intrinsic element directions, $\partial\theta/\partial\xi_j$, are

$$\frac{\partial\theta}{\partial \xi_j} = \sum_{n=1}^{8} \frac{\partial \Phi^n}{\partial \xi_j} \theta^n \tag{34}$$

which can relate to the temperature derivatives with respect to the global system, $\theta_{,k}$, as follows:

$$\frac{\partial\theta}{\partial \xi_j} = \frac{\partial\theta}{\partial x_k} \frac{\partial\theta}{\partial \xi_j} \tag{35}$$

6. BOUNDARY ELEMENT IMPLEMENTATION

Computation of the M_1-integral was included in the DBEM code as a post-processing procedure, and so it could be applied to the results from a particular model at a later stage. As it has been
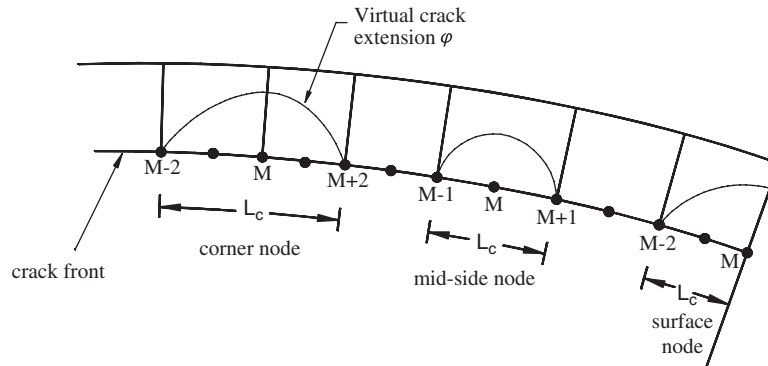
Figure 5. Schematic of the crack-front region illustrating the virtual crack extensions for a corner node, a mid-node and a surface node.
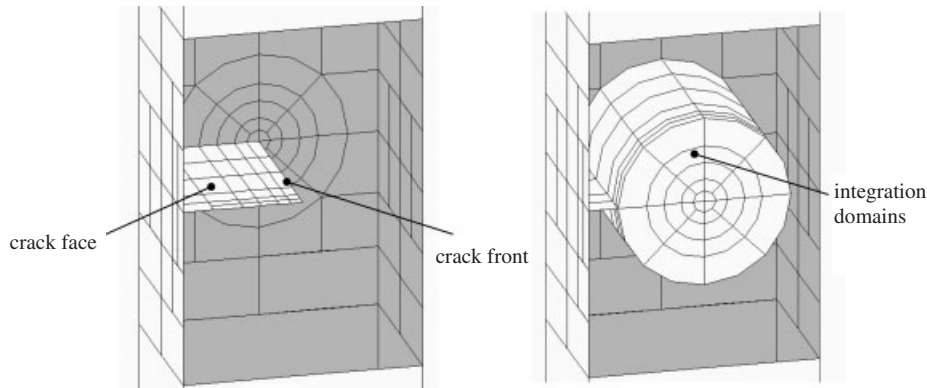

Figure 6. Boundary element discretization and integration cells.

stated in Sections 2 and 3, Equation (12) allows computation of the M_1-integral at any position η on the crack front. This requires the evaluation of a volume integral within domains that enclose a segment of the crack front L_c. A natural choice here is to make η coincident with the element nodes on the crack front, while L_c is taken as the element or element sides at which points η lies (see Figure 5).

The portion of the model domain in which the volume integrals are evaluated is discretized using 20-noded isoparametric (brick) cells, over which stresses, strains and displacements and temperature derivatives are approximated by products of the cell interpolation functions, Ψ^n, and the nodal values of σ_{ij}, ε_{ij}, u_{ij} and $\theta_{,k}$. Nodal values of these variables are computed following the procedures introduced in Sections 5.1 and 5.2 depending on whether the node is internal or lies on the model boundary. Volume discretization is designed to have a web-style geometry around the crack front, while the integration volumes are taken to coincide with different rings of cells. This is illustrated for an example in Figure 6, where one of the model faces has been removed to show the crack and the integration domains.

As depicted in Figure 5, three different cases need to be considered, depending on whether the node of interest M is in the middle of an element side (mid-node) is shared by two elements (corner node) or is located coincident with the external surface (surface node). If the node M is a mid-node or surface node, L_c (the segment of the crack front over which the J-integral is computed) spans over one element, connecting nodes $M - 1$, M and $M + 1$ and nodes $M - 2$, $M - 1$ and M, respectively. On the other hand, if M is a corner node, L_c spans over two elements, connecting nodes from $M - 2$ to $M + 2$.

Function φ is specified at all nodes within the integration volumes. Consistent with the isoparametric formulation, φ is given by

$$\varphi_k = \sum_{i=1}^{20} \Psi^i \varphi_k^i \tag{36}$$

where Ψ^i are the shape functions defined within each volume cell and φ_k^i are the nodal values for the ith node. From the definition of φ (see Equation (5)), $\varphi_k^i = 0$ if the ith node is on S_1, while for nodes inside V φ_k^i are given by interpolating between the nodal values on L_c and S_1.

Following standard manipulations,

$$\varphi_{k,j} = \sum_{i=1}^{20} \sum_{n=1}^{3} \frac{\partial \Psi^i}{\zeta_n} \frac{\partial \zeta_n}{\partial x_j} \varphi_k^i \tag{37}$$

where ζ_k are the coordinates in the cell isoparametric space.

If Gaussian integration is used, the discretized form of Equation (12) is given by

$$
\begin{aligned}
M_1 = \sum_{\text{cells in } V} \sum_{p=1}^{m} &\left\{ [(\sigma_{ij}^{*(1)} u_{j,k}^{*(2)} + \sigma_{ij}^{*(2)} u_{j,k}^{*(1)} - \sigma_{ij}^{*(1)} \varepsilon_{ij}^{*(2)} \delta_{ki}) \varphi_{k,i} \right. \\
&\left. + \sigma_{nn}^{*(2)} \alpha \theta_{,k}^{(1)} \varphi_k] \det\left(\frac{\partial x_j}{\partial \xi_k} \right) \right\}_p w_p
\end{aligned}
\tag{38}
$$

where m is the number of Gaussian points per cell, and w_p are the weighting factors.

The auxiliary function φ was introduced in the derivation of EDI in order to model the virtual crack-front advance. Since the virtual crack advance can adopt any arbitrary shape, the only requirement for the function φ is to be sufficiently smooth within the integration volume V as the evaluation of the EDI requires its differentiation. Although Shih *et al.* [15] have shown that the J values computed using the EDI are insensitive to the assumed shape of the φ function, the authors' experience shows that the shape of the function φ could be relevant for the performance of the computations.

Figure 7 illustrates a number of usual definitions for the function φ, namely linear, quadratic and plateau-type functions. The quadratic definition of φ has been employed with excellent results in previous works by Cisilino and co-workers [22–24] when dealing with problems without body forces. The excellent performance of this definition of φ could be explained by its behaviour in the region close to the crack tip. Note that the gradient $\varphi_{,i}$ of the quadratic function is very low in the vicinity of the crack front (region close to the coordinate $r/r_0 = 0$ in Figure 7), which results in marginal contribution of the crack-front fields to the overall result (see the first term of the integral in Equation (12)). In this way, the zone of the integration domain with the lowest accuracy for the actual field has a minimum contribution to the computed result. As it is easy to
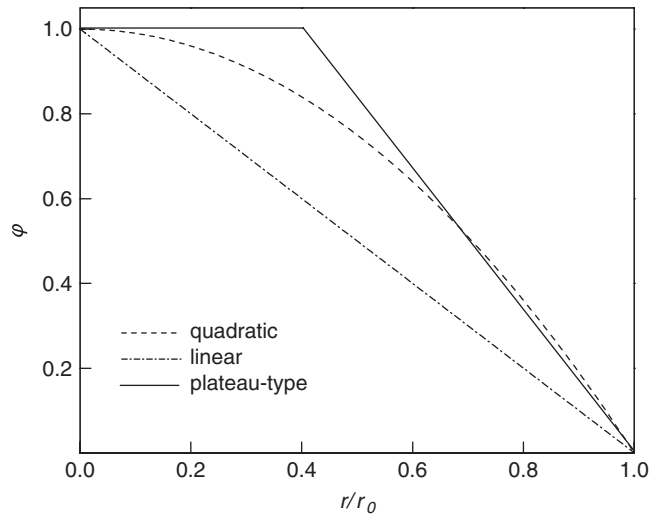
Figure 7. Alternatives for the selection of the φ function.

see, the linear definition of φ does not possess this benefit. Besides, it could be argued that the plateau-type function should maximize the previous mentioned benefit; however, it was found that the discontinuous definition of the function attempts to the accuracy of the computations.

Within this approach, φ is defined to vary quadratically in the directions tangential and normal to the crack front. Considering that the evaluation point η is at the middle of the crack-front segment L_c, and r_0 is the radius of the integration domain, the function φ is written as

$$\varphi(x) = \left\| 1 - \left(\frac{x_3}{L_c/2} \right)^2 \right\| \cdot \left[1 - \left(\frac{r}{r_0} \right)^2 \right] \tag{39}$$

where r is the distance from the crack front in the $x_1 - x_2$ plane as depicted in Figure 1.

Finally, it is important to mention that the above discussion about the selection of φ rests on the application of the M_1-integral to the solution of problems without body loads. Under these circumstances the second term of the integral in Equation (12), the term that accounts for body loads (thermal loads in our case), vanishes. On the other hand, when dealing with body loads, the second term in the integrand of Equation (12) has to be considered. Note that this term is multiplied by the function φ itself and not its gradient $\varphi_{,i}$, so that the justification given in the previous paragraph for the performance of the quadratic definition of the function is in this case not complete. However, excellent results were obtained by the authors when using the bi-quadratic definition of φ in the computation of the J-integral in thermoelastic problems using the EDI [25].

7. EXAMPLES

Results for three examples are presented in this section in order to demonstrate the efficiency and accuracy of the proposed implementation. In every case material properties are Young's modulus

$E = 100\,000\,\text{N/mm}^2$, Poisson ratio $v = 0.3$, coefficient of thermal expansion $\alpha = 10^{-5}/°\text{C}$ and thermal conductivity $\lambda = 1\,\text{W}/°\text{C mm}$.

7.1. Thick panel with a centre slant crack subjected to a linear thermal field

This example consists in a thick panel with a centre slant crack of length $2a$ inclined 30° with respect to the horizontal. The panel dimensions are length $2L = 8a$, width $2W = 4a$ and thickness $t = 3a$ (see Figure 8). The specimen is subjected to a linear temperature variation throughout the width $2W$, with temperature $\theta_0 = -100°\text{C}$ specified over the specimen's left lateral face ($x = 0$) and $\theta_1 = 0°\text{C}$ over the right lateral face ($x = W$). All other surfaces of the specimen (including the crack faces) are isolated. Displacements at the bottom and top surfaces of the bar are restricted in the y direction; all other surfaces are allowed to move freely.

The symmetry of the problem with respect to the plane $z = 0$ (see Figure 8) allowed discretizing half of the specimen only. Symmetry boundary conditions were imposed by restricting the displacements of the specimen's back surface in the z direction. The model discretization was constructed using 1989 nodes and 401 elements. Crack-front element dimensions were graded towards the free surface, the smallest one being equal to $t/32$. Four rings or cells with radii $r/a = 0.2, 0.35, 0.5$ and 0.75 were accommodated around the crack fronts for K-computations. With this purpose 432 cells and 2556 were employed. Figure 9 depicts the deformed specimen together with the temperature contour plots.

Computed K results for the two crack fronts are plotted in Figure 10, while in Tables I and II the results are presented in tabular form for the crack front 2 only. The columns labelled 'Dispersion'
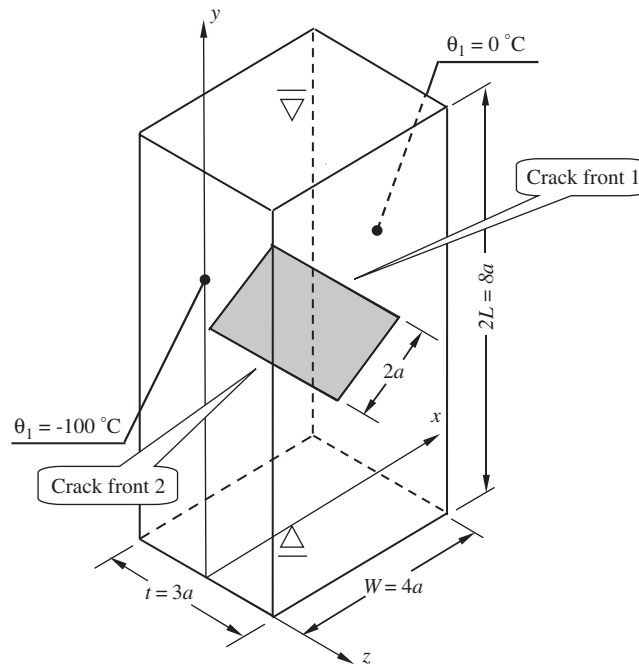

Figure 8. Geometry, dimensions and boundary conditions for the centre slant crack in a thick panel.
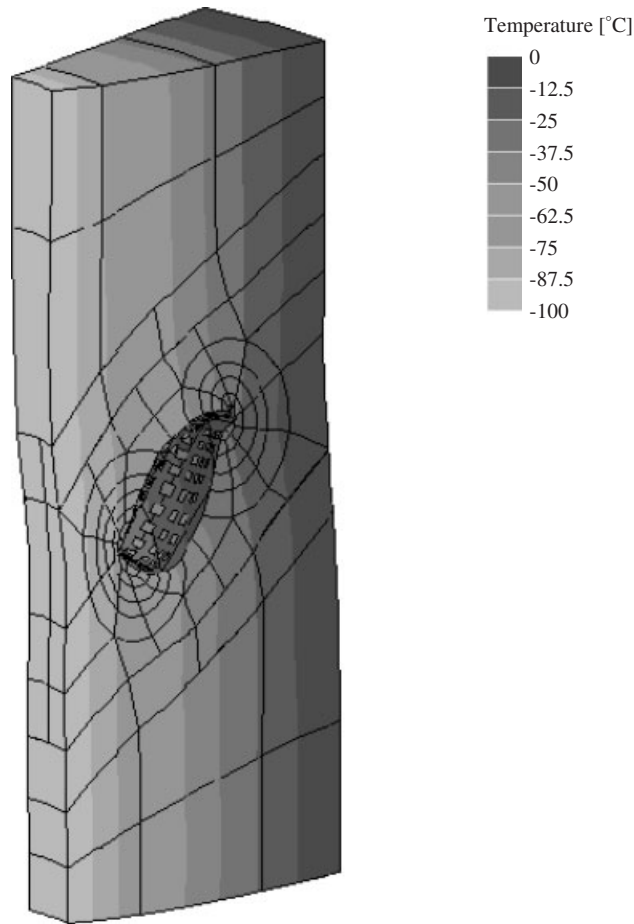
Figure 9. Deformed specimen and temperature plots for the slant crack in the thick panel.

in the tables serve to assess the path independence of the K computations, as they indicate the dispersion of the results obtained using the four integration paths. Also included as reference in Figure 10 is a set of results computed using a two-dimensional plane-stress FEM model. The FEM model was solved using Abaqus [41]. In every case, K results are normalized with respect to $F = (E/(1 - v))\alpha\theta_1\sqrt{\pi/a}$.

Figure 10 shows that, with the only exception of the region close to the free surface, K results are almost constant along the crack fronts. These constant K values in the interior of the specimen are in close agreement with those computed using the two-dimensional FEM model. On the other hand, the K_I values fall at the free surface while K_{II} values rise. This behaviour is also observed when solving a specimen of similar characteristics subjected to mechanical tractions [37, 42]. The results in Table I show that the computed K_I results are almost independent of the integration path, with dispersion less than 1% for all positions of the crack front, with the only exception of the point located at the intersection of the crack front with the free surface which exhibits a dispersion of
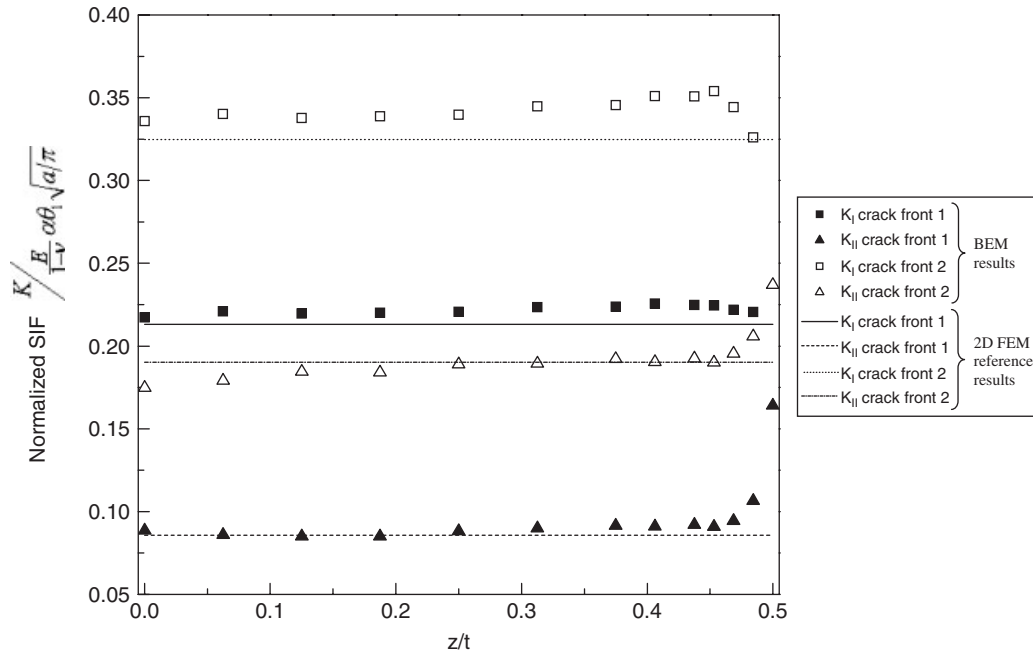
Figure 10. Normalized stress intensity factor results along the two crack fronts
of the slant crack in the thick panel.

Table I. Normalized K_I results for crack front #2 of the slant crack in the thick panel.

	r/a					
z/t	0.20	0.35	0.50	0.75	Average	Dispersion (%)
0.0000	0.3332	0.3379	0.3375	0.3348	0.3358	0.67
0.0625	0.3419	0.3417	0.3401	0.3367	0.3401	0.71
0.1250	0.3369	0.3390	0.3384	0.3364	0.3377	0.37
0.1875	0.3394	0.3395	0.3387	0.3377	0.3388	0.25
0.2500	0.3373	0.3406	0.3408	0.3403	0.3398	0.48
0.3125	0.3448	0.3453	0.3449	0.3444	0.3449	0.12
0.3750	0.3426	0.3463	0.3467	0.3469	0.3456	0.59
0.4063	0.3508	0.3514	0.3509	0.3507	0.3510	0.09
0.4375	0.3474	0.3513	0.3519	0.3525	0.3508	0.66
0.4531	0.3538	0.3544	0.3540	0.3539	0.3540	0.07
0.4688	0.3425	0.3453	0.3451	0.3442	0.3443	0.37
0.4844	0.3301	0.3278	0.3251	0.3214	0.3261	1.15
0.5000	0.2254	0.1241	0.0073	0.2054	0.1406	70.45

around 70%. In this sense it is worth noting that the formulation of M_1-integral methodology used
in this work is based on the assumption that the near-crack tip fields asymptote to the plane strain
fields along the complete crack front. But it turns out that at the intersection of the crack front and

Table II. Normalized K_{II} results for crack front #2 of the slant crack in the thick panel.

	r/a					
z/t	0.20	0.35	0.50	0.75	Average	Dispersion (%)
0.0000	0.1641	0.1733	0.1780	0.1840	0.1749	4.80
0.0625	0.1645	0.1778	0.1839	0.1907	0.1792	6.21
0.1250	0.1779	0.1834	0.1865	0.1902	0.1845	2.82
0.1875	0.1790	0.1839	0.1860	0.1878	0.1842	2.06
0.2500	0.1883	0.1890	0.1894	0.1894	0.1890	0.28
0.3125	0.1871	0.1904	0.1907	0.1899	0.1895	0.86
0.3750	0.1938	0.1930	0.1921	0.1901	0.1922	0.83
0.4063	0.1901	0.1921	0.1912	0.1885	0.1905	0.82
0.4375	0.1961	0.1941	0.1920	0.1882	0.1926	1.75
0.4531	0.1915	0.1924	0.1904	0.1862	0.1901	1.45
0.4688	0.1980	0.1984	0.1956	0.1902	0.1955	1.92
0.4844	0.1997	0.2096	0.2090	0.2054	0.2059	2.20
0.5000	0.2281	0.2408	0.2425	0.2364	0.2370	2.72

the free surface the stress singularity is more severe than the usual $1/\sqrt{r}$, which invalidates the implemented methodology. Similar results are reported in References [28, 31]. K_{II} results reported in Table II present similar levels of dispersion along the complete crack front, including the point at the intersection with the free surface. Although still reasonably low, the dispersion for the K_{II} results is higher than that for K_I. The results for crack front #1 present a behaviour identical to that reported for crack front #2.

7.2. Penny-shaped crack in a circular bar

This example consists in a cylindrical bar containing a penny-shaped crack, as illustrated in Figure 11(a). Model dimensions are crack radius $a = 10$ mm, cylinder radius $R/a = 10$ and cylinder height $h/R = 6$. The relatively large dimensions of the bar with respect to the dimensions of the crack allow assimilating this example to that of a circular crack in an infinite solid. Two loading configurations were considered with the crack oriented parallel to the bar ends ($\alpha = 0$), and rotated $\alpha = 30°$ and 45°. The model was discretized using 1434 nodes and 224 elements, 152 of which are used for the crack faces (see Figure 11(b)). Three rings of cells constructed using 4352 nodes and 832 cells with radii $r/a = 0.2, 0.35$ and 0.50 were used for the K computations.

The first loading case consists in a penny-shaped crack with crack-surface temperature $\theta_0 = 100°C$ embedded in an infinite solid with temperature $\theta_1 = 0°C$. This problem results in a pure mode-I solicitation for the crack, irrespective of the crack orientation. The analytical solution for this problem is due to Olesiak and Sneddon [43]:

$$K_0 = \frac{E\alpha}{\pi^{1/2}(1-v)}\theta_0\sqrt{a} \tag{40}$$

To model this problem the crack-surface temperature in the BEM model was set to $\theta_0 = 100°C$, while the temperatures for all the other external surfaces of the cylinder were set to $\theta_1 = 0°C$. Displacement boundary conditions at infinity were idealized using two approaches: (i) no displacement boundary conditions were imposed on the cylinder external surfaces (with the only exception
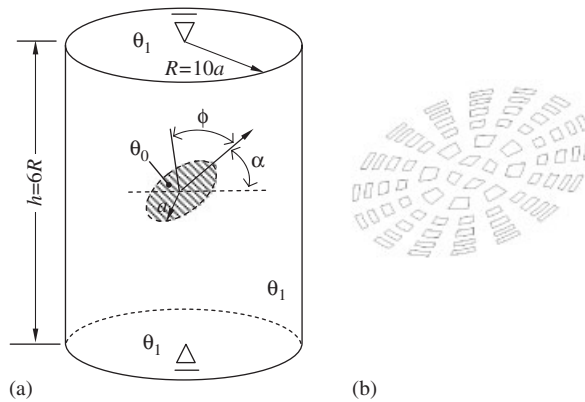
Figure 11. Circular crack in a cylindrical bar: (a) geometry, dimensions and boundary conditions (not to scale) and (b) crack discretization.

of those necessary to restrict the rigid body motions and rotations) and (ii) the displacements of the external surfaces were fully constrained. The normalized stress intensity factor computed for the first approach was $K_I/K_0 = 0.952$ (4.8% error with respect to the reference value), while for the second approach $K_I/K_0 = 0.992$ (0.8% error). In every case, the dispersion of the results for the different integration paths was less than 2%. These results allow concluding that, despite the relative large dimensions of the bar with respect to the size of the crack, the problem cannot be strictly assimilated with that of a crack in an infinite solid. Anyway, the performance of the implemented algorithm is validated.

For the second analysis a constant temperature field was imposed on the entire bar ($\theta_0 = \theta_1 = -100°C$), and the displacements of both ends of the bar were restricted to the longitudinal direction (see Figure 11(a)). Stress intensity factors were solved for the three crack orientations, $\alpha = 0, 30$ and $45°$. The above-mentioned boundary conditions allow assimilating the problem to that of a crack under remote uniform tension for which analytical solutions of stress intensity factors exist.

Results computed for the second analysis are reported in Figure 12. All results are given in terms of the angle ϕ which indicates the position along the crack front (see Figure 11(a)), and they are normalized with respect to the exact solution due to Sneddon [44] for the case of a penny-shaped crack under uniform tension

$$K_0 = 2\sigma\sqrt{\frac{a}{\pi}} \tag{41}$$

taking $\sigma = E\alpha\theta_0$, the magnitude of the constant stress field in the longitudinal direction for the case of the bar without a crack. Also included as a reference in Figure 12 are the analytical solutions due to Sneddon [44] and Kassir and Sih [45]. Computed results are in excellent agreement with those of the reference, exhibiting an error around 1%. Similar to the previous loading case, the dispersion of the results for the different integration paths was less than 2%.

7.3. Semicircular crack in a square bar

A prismatic bar with square section and dimensions $W = 2a$ and $L = 2W$ containing a semicircular crack of radius $a = 10$ mm is considered in this example. As illustrated in Figure 13, two
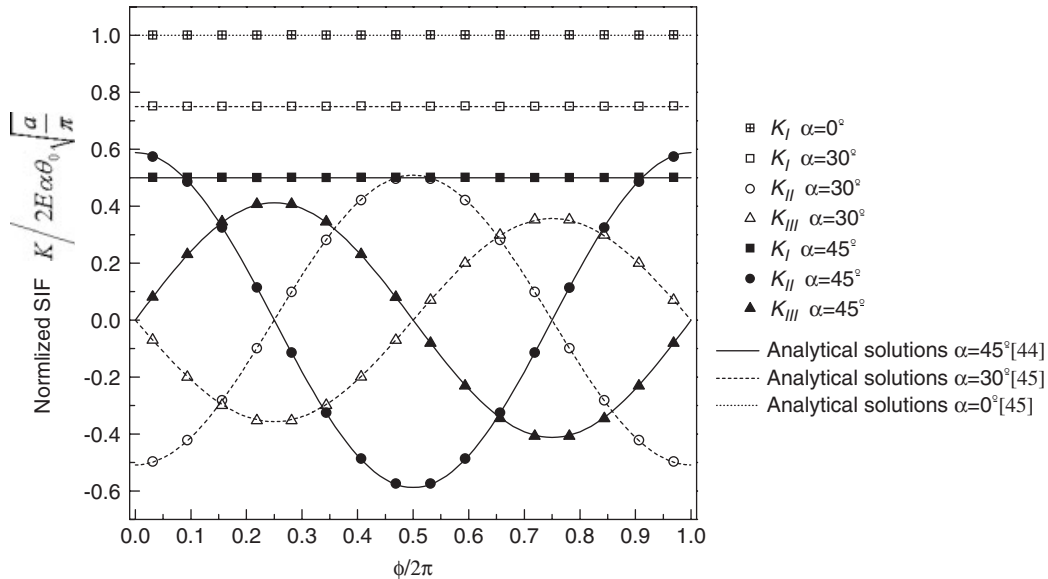
Figure 12. Circular crack in a cylindrical bar: normalized stress intensity factor results as a function of the position on the crack front position.

configurations for the crack are considered. In case (a) the crack is horizontal, parallel to the bar ends, while in case (b) it is rotated $45°$ with respect to the horizontal plane. The boundary element discretization consists of 1249 nodes and 260 elements, 76 of which are used for the crack faces. Internal cell discretization for K computations consists of 2374 nodes and 416 cells, which were used to construct three rings of cells with radii $r/a = 0.2, 0.50$ and 0.75, respectively.

Boundary conditions consist in a linear temperature variation in direction z with temperatures $\theta_0 = -100°C$ and $\theta_1 = 100°C$ specified for the front ($z = W$) and back faces ($z = 0$) of the specimens, respectively. All other surfaces of the specimen (including the crack faces) are isolated. Displacements at the bottom and top surfaces of the bar are restricted in the longitudinal (z) direction, while the lateral surfaces are allowed to move freely. This loading configuration results in a uniform bending moment in the x-direction. Figure 14 illustrates the deformed specimen together with the temperature contour plots for the two crack configurations.

Normalized stress intensity factor results are given in Figure 15 for both crack configurations. As expected, the horizontal crack is subjected to mode-I stress intensity factor only, while for the inclined crack the three K-modes are present. Path independence of the computed K-results was found to be very good. The major dispersion of the results occurred for the points located at the intersection of the crack front with the free surface (positions $\phi/\pi = 0$ and $\phi/2\pi = 1$ in Figure 15), where dispersions up to 7% for the K_I results can be found. As for the first example, the loss of dominance of the $1/\sqrt{r}$ singularity for the stress field at the free surface is the justification for this behaviour. On the other hand, the dispersion of the K_I results at interior points for both crack configurations, and the dispersions of the K_{II} and K_{III} results along the complete crack fronts (including at the free surfaces) for the inclined crack do not exceed 2% in any case.
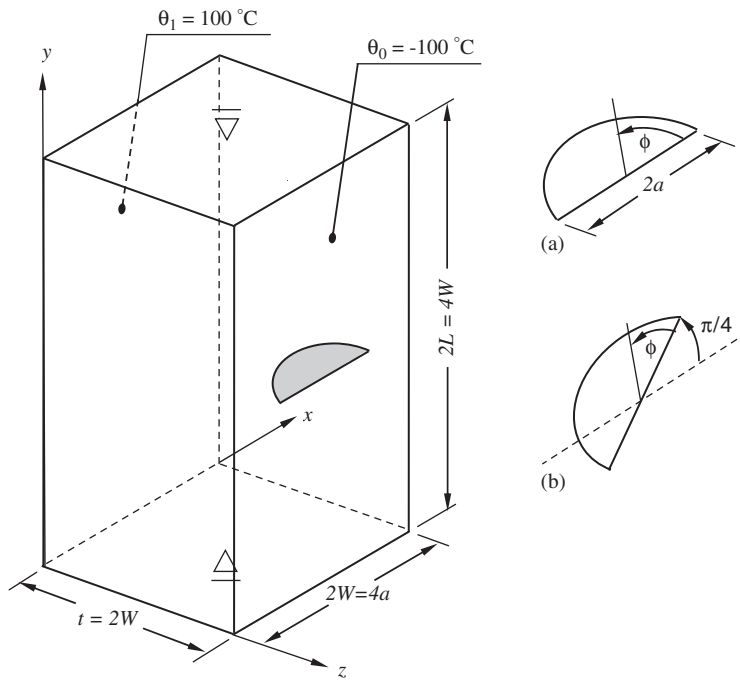
Figure 13. Geometry, dimensions and boundary conditions for the semicircular crack in a square bar:
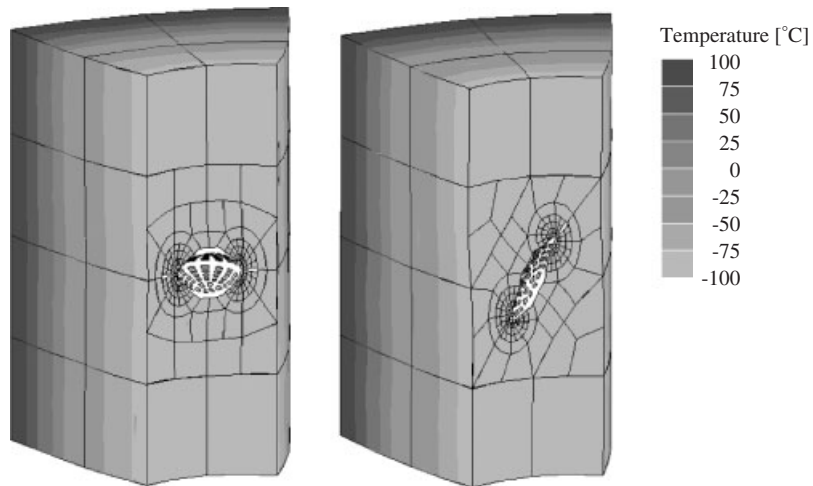(a) horizontal crack and (b) inclined crack.

Figure 14. Semicircular crack in a square bar: deformed specimen and
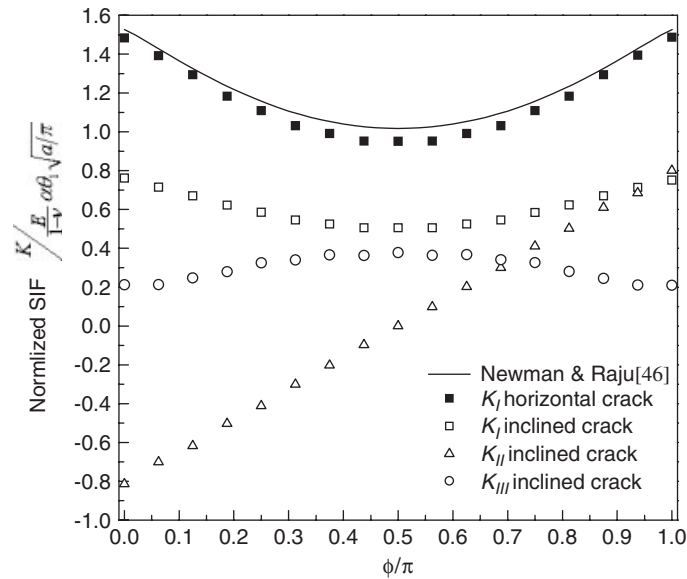temperature plots for the crack geometries.

Figure 15. Semicircular crack in a square bar: normalized stress intensity factors results along the crack fronts for the two crack geometries.

Also included in Figure 15 is a set of results calculated using the empirical equations due to Newman and Raju [46] for a semi-elliptical crack under pure bending. This set of results is compared with the K_I computations for the horizontal crack. The maximum difference between the two sets of results is 5.5%, and it occurs at the deepest point of the crack front ($\phi/\pi = 0.5$). Reported accuracy for the reference values is 5% of the finite element results used for the derivation of the empirical equations.

8. CONCLUSIONS

A dual boundary element method formulation of the M_1-integral methodology for the numerical computation of mixed-mode stress intensity factors of three-dimensional thermoelastic fracture problems has been presented in this paper. The implementation takes advantage of the efficiency of the boundary integral equations to directly obtain the required displacement and temperature derivatives, stress, strain and temperature fields. A number of examples have been solved to demonstrate the efficiency and accuracy of the proposed formulation.

Computed K results show a very good agreement with other results reported in the literature, with deviations of only a few percents. The same level of accuracy was obtained when using the energy domain integral for solving elastic, elastoplastic, thermoelastic and interface crack problems [22–25] using similar levels of mesh refinement. These results show the efficiency of the BEM implementation of the domain integral approaches to tackle general three-dimensional crack problems.

Maximum errors and dependence of the results with the integration paths occur at the points located at the intersection of the crack front with the free surface. It turns out that, at the intersection of the crack front and the free surface, the stress singularity is more severe than the usual $1/\sqrt{r}$, and thus the interaction integral methodology is not applicable. This problem remains unsolved in this work. Following previous work [37], alternative approaches for the selection of the auxiliary function φ could be explored to solve this problem.

Following Walters *et al.* [28], the interaction integral implemented in this work omits the terms arising due to the crack-front curvature, resulting in a simpler algorithm. The accuracy and path independence of the reported results provide further evidence in support of the capability of the simplified algorithm to yield accurate stress intensity factors with reasonable levels of mesh refinement.

APPENDIX

In this appendix, the fundamental solutions for the implementation of the thermoelastic formulation of the DBEM are provided. In what follows, the symbol r stands for the distance from the field point x to the source point x':

$$r(x', x) = |x - x'| \tag{A1}$$

The notation $r_{,k}$ indicates derivative at the source point, i.e.

$$\frac{\partial r}{\partial x_k} = -r_{,k} \tag{A2}$$

The fundamental solutions in the temperature equation (10) are

$$\theta^*(x', x) = \frac{-1}{4\pi r} \tag{A3}$$

$$q^*(x', x) = \lambda \frac{r_{,k} n_k}{4\pi r^2} \tag{A4}$$

The fundamental solutions for the flux equation (11) can be found after the differentiation of solutions (A3) and (A4) to yield

$$\theta_i^{**}(x', x) = \frac{\lambda}{4\pi r^2} r_{,i} \tag{A5}$$

$$q_i^{**}(x', x) = \frac{\lambda}{4\pi r^3} (3r_{,i} r_{,k} n_k - n_i) \tag{A6}$$

The fundamental solutions in the displacement equation (14) are given by

$$T_{ij}(x', x) = \frac{-1}{8\pi(1-v)r^2} \left\{ \frac{\partial r}{\partial n}[(1-2v)\delta_{ij} + 3r_{,i}r_{,j}] - (1-2v)(n_j r_{,i} - n_i r_{,j}) \right\} \tag{A7}$$

$$U_{ij}(x', x) = \frac{-1}{16\pi(1-v)\mu r} \{(3-4v)\delta_{ij} + r_{,i} r_{,j}\} \tag{A8}$$

$$\overline{P}_i(x', x) = \frac{\alpha(1+v)}{8\pi(1-v)r}\left(n_i - \frac{\partial r}{\partial n}r_{,i}\right) \tag{A9}$$

$$\overline{Q}_i(x', x) = \frac{\alpha(1+v)}{8\pi(1-v)}r_{,i} \tag{A10}$$

The fundamental solutions in the traction equation (15) are obtained by differentiating expressions (A7)–(A10) and by applying the material constitutive relationships. This procedure gives

$$T_{kij}(x', x) = \frac{\mu}{4\pi(1-v)r^3}\left\{3\frac{\partial r}{\partial n}[(1-2v)\delta_{ij}r_{,k} + v(\delta_{ij}r_{,k} + \delta_{jk}r_{,i} - 5r_{,i}r_{,j}r_{,k})]\right.$$
$$+ 3v(n_i r_{,j}r_{,k} + n_j r_{,i}r_{,k}) + (1-2v)(3n_k r_{,i}r_{,j} + n_k\delta_{ij} + n_i\delta_{jk})$$
$$\left. - (1-4v)n_k\delta_{ij}\right\} \tag{A11}$$

$$U_{kij}(x', x) = \frac{1}{8\pi(1-v)r^2}[(1-2v)(\delta_{ik}r_{,j} + \delta_{jk}r_{,i} - \delta_{ij}r_{,k}) + 3r_{,i}r_{,j}r_{,k}] \tag{A12}$$

$$\overline{P}_{ij}(x', x) = 4\frac{\alpha\mu(1+v)}{8\pi(1-v)r^2}\left\{n_k r_{,k}\left[\frac{\delta_{ij}}{1-2v} - 3r_{,i}r_{,j}\right] + n_i r_{,j} + n_j r_{,i}\right\} \tag{A13}$$

$$\overline{Q}_i(x', x) = 4\frac{\alpha\mu(1+v)}{8\pi(1-v)r}\left(r_{,i}r_{,j} - \frac{\delta_{ij}}{1-2v}\right) \tag{A14}$$

REFERENCES

1. Murakami Y (ed.). *Stress Intensity Factor Handbook*. Pergamon Press: Oxford, U.K.,
2. Tada H, Paris PC, Irwin GR. *The Stress Analysis of Cracks Handbook* (3rd edn). ASME Press: New York, 2000.
3. Brebbia CA, Telles JCF, Wrobel LC. *Boundary Element Techniques*. Springer: Berlin, 1984.
4. Aliabadi MH. Boundary element formulations in fracture mechanics. *Applied Mechanics Review* 1997; **50**:83–96.
5. Raveendra ST, Banerjee PK. Boundary element analysis of cracks in thermally stressed planar structures. *International Journal of Solids and Structures* 1992; **29**:2301–2317.
6. Mukherjee YX, Shah K, Mukherjee S. Thermoelastic fracture mechanics with regularized hypersingular boundary integral equations. *Engineering Analysis with Boundary Elements* 1999; **23**:89–96.
7. Prasad NNV, Aliabadi MH, Rooke DP. The dual boundary element method for thermoelastic crack problems. *International Journal of Fracture* 1994; **66**:255–272.
8. dell'Erba, Aliabadi MH. BEM analysis of fracture problems in three-dimensional thermoelasticity using *J*-integral. *International Journal of Solids and Structures* 2001; **38**:4609–4630.
9. dell'Erba D, Aliabadi MH. Three-dimensional thermo-mechanical fatigue crack growth using BEM. *International Journal of Fatigue* 2000; **22**(4):261–273.
10. Aliabadi MH, Rooke DP. *Numerical Fracture Mechanics*. Computational Mechanics Publications, Kluwer Academic Publishers: Southampton, U.K., Dordrecht, The Netherlands, 1992.

11. Rice JR. A path independent integral and the approximate analysis of strain concentration by notches and cracks. *Journal of Applied Mechanics* 1968; **35**:379–386.
12. Hellen TK. On the method of virtual crack extensions. *International Journal for Numerical Methods in Engineering* 1975; **9**:187–207.
13. Parks DM. A stiffness derivative finite element technique for determination of elastic crack tip stress intensity factors. *International Journal of Fracture* 1974; **10**:487–502.
14. Carpenter WC, Read DT, Dodds RH. Comparison of several path independent integrals including plasticity effects. *International Journal of Fracture* 1986; **31**:303–323.
15. Shih CF, Moran B, Nakamura T. Energy release rate along a three-dimensional crack front in a thermally stressed body. *International Journal of Fracture* 1986; **30**:79–102.
16. Blackburn WS. Path independent integrals to predict onset of crack instability in an elastic plastic material. *International Journal of Fracture* 1972; **8**:343–346.
17. Ainsworth RA, Neal BK, Price RH. Fracture behaviour in the presence of thermal strains. *Proceedings of the Institute of Mechanical Engineers*, *Conference on Tolerance of Flaws in Pressurised Components*, London, 1978.
18. Wilson WK, Yu IW. The use of *J*-integral in thermal stress crack problems. *International Journal of Fracture* 1979; **15**:377–387.
19. Kishimoto K, Auki S, Sakata M. On the path independent integral-*J*. *Engineering Fracture Mechanics* 1980; **13**:841–850.
20. Auki S, Kishimoto K, Sakata M. Elastic–plastic analysis of crack in thermally loaded structures. *Engineering Fracture Mechanics* 1982; **16**:405–413.
21. Rigby RH, Aliabadi MH. Decomposition of the mixed-mode *J*-integral—revisited. *International Journal of Solids and Structures* 1998; **35**:2073–2099.
22. Cisilino AP, Aliabadi MH, Otegui JL. Energy domain integral applied to solve center and double-edge crack problems in three-dimensions. *Theoretical and Applied Fracture Mechanics* 1998; **29**:181–194.
23. Cisilino AP, Aliabadi MH. BEM implementation of the energy domain integral for the elastoplastic analysis of 3D fracture problems. *International Journal of Fracture* 1999; **96**:229–245.
24. Cisilino AP, Ortiz JE. Three-dimensional boundary element assessment of fibre/matrix interface cracks under transverse loading. *Computers and Structures* 2005; **83**:856–869.
25. Balderrama R, Cisilino AP, Martinez M. BEM analysis of three-dimensional fracture problems using the energy domain integral. *Journal of Applied Mechanics* (ASME) 2006; **73**(6):959–969.
26. Li FZ, Shih CF, Needleman A. A comparison of methods for calculating energy release rates. *Engineering Fracture Mechanics* 1985; **21**:405–421.
27. Natha R, Moran B. Domain integrals for axisymmetric interface crack problems. *International Journal of Solids and Structures* 1993; **30**(15):2027–2040.
28. Walters MC, Paulino GH, Dodds RH. Interaction integral procedures for 3-D curved cracks including surface tractions. *Engineering Fracture Mechanics* 2005; **72**:1635–1663.
29. Williams ML. On the stress distribution at the base of a stationary crack. *Journal of Applied Mechanics* (ASME) 1957; **24**:109–114.
30. Yau JF, Wang SS, Corten HT. A mixed-mode crack analysis of isotropic solids using conservation laws of elasticity. *Journal of Applied Mechanics* (ASME) 1980; **4**:335–341.
31. Gosz M, Moran B. An interaction energy integral method for computation of mixed-mode stress intensity factors along nonplanar crack fronts in three dimensions. *Engineering Fracture Mechanics* 2002; **69**:299–319.
32. Kim YJ, Kim H-G, Im S. Mode decomposition of three-dimensional mixed-mode cracks via two-state integrals. *International Journal of Solids and Structures* 2001; **38**:6405–6426.
33. Cho YJ, Beom HG, Earmme YY. Application of a conservation integral to an interface crack interacting with singularities. *International Journal of Fracture* 1994; **65**:63–73.
34. Gosz M, Dolbow J, Moran B. Domain integral formulation for stress intensity factor computation along curved three dimensional interface cracks. *International Journal of Solids and Structures* 1998; **35**:1763–1783.
35. Nakamura T, Parks DM. Determination of elastic T-stress along three-dimensional crack fronts using an interaction integral. *International Journal of Solids and Structures* 1992; **29**:1597–1611.
36. Miyazaki N, Ikeda T, Soda T, Munakata T. Stress intensity factor analysis of interface crack using boundary element method—application of contour-integral method. *Engineering Fracture Mechanics* 1993; **45**(5):599–610.
37. Cisilino AP, Ortiz JE. Boundary element analysis of three-dimensional mixed-mode cracks via the interaction integral. *Computer Methods in Applied Mechanics and Engineering* 2005; **194**(9–11):935–956.
38. Ortiz JE, Cisilino AP. Boundary element method for *J*-integral and stress intensity factor computations in three-dimensional interface cracks. *International Journal of Fracture* 2005; **133**:197–222.

39. Knowles JK, Sternberg E. On a class of conservation laws in linearized and finite elastostatics. *Archive for Rational Mechanics and Analysis* 1972; **7**:55–129.
40. Sih GC. On the singular character of thermal stress near a crack tip. *Journal of Applied Mechanics* 1962; **29**:587–589.
41. ABAQUS Standard 6.5. Providence, RI, U.S.A., 2006.
42. Raju IS, Newman JC. Three-dimensional finite-element analysis of finite-thickness fracture specimens. *Technical Report NASA TN D-8414*, 1977.
43. Olesiak Z, Sneddon IN. The distribution of thermal stress in a infinite elastic solid containing a penny-shaped crack. *Archive for Rational Mechanics and Analysis* 1959; **4**:238–254.
44. Sneddon IN. The distribution of stress in the neighbourhood of a crack in an elastic solid. *Proceedings of Royal Society of London*, *Series A* 1946; **187**:229–260.
45. Kassir MK, Sih GC. Three dimensional stress distribution around an elliptical crack under arbitrary loadings. *Transactions of ASME*, *Journal of Applied Mechanics* 1966; **33**:601–611.
46. Newman JC, Raju IS. An empirical stress intensity factor equation for the surface crack. *Engineering Fracture Mechanics* 1986; **15**(1–2):185–192.